Mixed model phase evolution for correction of magnetic field inhomogeneity effects in 3D quantitative gradient echo-based MRI

Chemseddine Fatnassi[a)]
Division of Nuclear Medicine and Molecular Imaging, Geneva University Hospital, CH-1211 Geneva, Switzerland
Radio-Oncology Institute, Clinique Bois-Cerf Hirslanden, CH-1006 Lausanne, Switzerland

Rachid Boucenna
Radio-Oncology Institute, Clinique Bois-Cerf Hirslanden, CH-1006 Lausanne, Switzerland

Habib Zaidi
Division of Nuclear Medicine and Molecular Imaging, Geneva University Hospital, CH-1211 Geneva, Switzerland
Geneva Neuroscience Centre, Geneva University, CH-1205 Geneva, Switzerland
Department of Nuclear Medicine and Molecular Imaging, University of Groningen, University Medical Center Groningen, 9700RB Groningen, Netherlands
Department of Nuclear Medicine, University of Southern Denmark, DK-500 Odense, Denmark

Purpose: In 3D gradient echo magnetic resonance imaging (MRI), strong field gradients $B0_{macro}$ are visually observed at air/tissue interfaces. At low spatial resolution in particular, the respective field gradients lead to an apparent increase in intravoxel dephasing, and subsequently, to signal loss or inaccurate R_2^* estimates. If the strong field gradients are measured, their influence can be removed by postprocessing.

Methods: Conventional corrections usually assume a linear phase evolution with time. For high macroscopic gradient inhomogeneities near the edge of the brain and at the paranasal sinuses, however, this assumption is often broken. Herein, we explored a novel model that considers both linear and stochastic dependences of the phase evolution with echo time in the presence of weak and strong macroscopic field inhomogeneities. We tested the performance of the model at large field gradients using simulation, phantom, and human *in vivo* studies.

Results: The performance of the proposed approach was markedly better than the standard correction method, providing a correction equivalent to that of the conventional approach in regions with high signal to noise ratio (SNR > 10), but appearing more robust in regions with low SNR (SNR < 4).

Conclusion: The proposed technique shows promise to improve R_2^* measurements in regions of large susceptibilities. The clinical and research applications still require further investigation. © *2017 American Association of Physicists in Medicine* [https://doi.org/10.1002/mp.12318]

1. INTRODUCTION

Quantitative magnetic resonance imaging (MRI) by means of T_2^* relaxometry is becoming an increasingly useful tool in a number of clinical and research applications. The effective transverse relaxation rate $R_2^*(1/T_2^*)$ characterizes static magnetic field variations at the mesoscopic level,[1,2] which can be associated with local concentrations of paramagnetic macromolecules that may reveal the physiology of disordered brain function.[3] R_2^* is one of the principal determinants of image contrast in gradient echo-based sequences (GRE) and constitutes the basis for many MRI applications, such as susceptibility-weighted imaging (SWI) and quantitative susceptibility mapping (QSM) for accurate brain,[4–6] heart,[7] and liver[8] iron assessment. It is also applied for blood oxygenation level-dependent (BOLD) studies,[9,10] as well as for dynamic susceptibility contrast MRI,[11,12] cerebral venous blood volume measurement,[13] and detection of brain abnormalities, such as multiple sclerosis.[14] At high field ($\geq$ 3T), susceptibility-induced macroscopic field inhomogeneities, or macroscopic field gradients ($B0_{macro}$), increase the intravoxel dephasing in GRE MRI, leading to an apparent increase in the signal decay. The presence of $B0_{macro}$ leads to regions of no or low signal and inaccurate R_2^* quantification, which is regionally dependent and limits the reliability of the diagnostic interpretation of increased signal decay.

Numerous preprocessing and postprocessing methods have been proposed to correct for $B0_{macro}$ intravoxel dephasing. Preprocessing techniques aim to correct the magnitude data or compensate for $B0_{macro}$ by manipulating the slice selection gradient[15] or radiofrequency pulses.[16] Postprocessing techniques aim to remove the influence of the field gradient by estimating the extent of intravoxel dephasing. For 2D GRE imaging, Seara and Wehrli[17] proposed an iterative postprocessing technique to correct for the generated Sinc modulation by including a linear dephasing gradient in the slice direction. Their method was further optimized by Dahnke et al.[18] and Zeng et al.,[19] who introduced a point spread function method to correct the image distortion that occurs in echo planar imaging (EPI); however, this technique requires

an additional phase encoding acquisition. More complex analysis of the signal behavior generated by nonlinear spatial gradient inhomogeneities was investigated by Yang et al.[3] They derived an analytical solution to correct for the quadratic gradient through each slice and demonstrated that their technique is of particular importance for low resolution imaging (where the slice thickness is much greater than the in-plane resolution). Hernando et al.[20] introduced a method to correct for macroscopic field inhomogeneities in the presence of fat, whereby they used a third-order polynomial to model the field variations while the modulation term was calculated numerically. Lastly, Yablonskiy et al.[2] introduced the voxel spread function model, based on linear gradient evolution across the voxel to correct for the magnetic field inhomogeneity in quantitative GRE imaging.

In regions with high signal to noise ratio (SNR) and low susceptibility, such as the center of the brain, the algorithms mentioned above remove field inhomogeneity variation artifacts from the R_2^* maps. In regions with low SNR and high susceptibility artifacts, however, such as near the paranasal sinuses, most algorithms fail or overcorrect the images. This is likely due to either the choice of the field variation model across the image voxels or the phase evolution as a function of echo times. Regarding the first problem, the ideal combination of the polynomial fit order and the number of voxel neighbors reduces the fitting noise and consequently increases the accuracy of correction. Previous studies have shown that the choices of voxel neighbors and fit order are strongly dependent on the image resolution.[2,20] As such, blindly increasing these parameters may lead to fitting noise rather than increasing accuracy. Regarding the phase evolution, all of these methods assume that the phase evolves linearly as a function of time. Zeng et al.,[19] however, used simulation and *in vivo* studies to demonstrate that the linear assumption is broken in the presence of a large field gradient, which is in agreement with our observations of images produced using a 3T MRI, where the effect of susceptibility-induced $B0_{macro}$ is expected to be worse. To the best of our knowledge, none of the models proposed to date account for the observed change in phase evolution with time.[21] We hypothesize that the observed overcorrection, e.g., near the paranasal sinuses, is due to the linear phase evolution assumption being broken. Hence, the phase loses linearity, appears random, and evolves without following any known nonlinear model (quadratic, cubic, or high-order behavior). Consequently, the phase jump may be difficult to detect and to correct for.

In this work, we re-examine the influence of macroscopic field inhomogeneities on multi-echo GRE signal formation, and propose an analytical mixed model solution for accurate phase dispersion estimation over echo time, which takes into account both linear and stochastic temporal phase behaviors. The linear part of the model utilizes the same approximation described in previous works,[17,18] whereas the stochastic component is based on the principles of random walk theory,[22–26] which allows accurate quantitative correction in the presence of extremely large field gradients. This approach, referred to as mixed model Sinc correction (MMSC), combines the

linear gradient behavior across an image voxel, and both linear and stochastic phase behavior as a function of echo time. The proposed technique can be applied to a variety of GRE pulse sequences used for acquiring quantitative images.

In the following section, we will briefly review the fundamental principles of linear correction models, which assume a linear evolution of phase with time. For a more complete description, we refer interested readers to Refs. [1,2,17]. The theory will then be expanded to consider a stochastic phase evolution with time; we also introduce a new method enabling accurate field map generation. The proposed approach will be validated using simulation, experimental phantom, and *in vivo* studies. A comparison with the noniterative 3D linear Sinc correction (LSC) method[17,18] is also provided.

2. THEORY

The MRI signal in a 3D gradient echo experiment for a given n^{th} voxel acquired in the presence of inhomogeneous magnetic field ΔB_n that is assumed to be equivalent through all vector position directions $\vec{r}$ can be written as:

$$S_n(k; TE_N) = \int_{-\infty}^{+\infty} \rho_n(\vec{r}, TE_N) \cdot \exp\{-2i\pi k\vec{r}\} \cdot F_n(\vec{r}, TE_N) d\vec{r} \tag{1}$$

where $\rho_n(\vec{r}, TE_N)$ is the ideal signal decay in the absence of field inhomogeneities, N is the echo number, and TE is the echo time. $F_n(\vec{r}, TE_N) = \exp(-i\Delta\phi(\vec{r}, TE_N))$ describes the signal loss due to the macroscopic $\Delta B_n(\vec{r})$ inhomogeneities and the k-Space is defined conventionally as:

$$2\pi k_x = \gamma G_x t_x \quad 2\pi k_y = \gamma G_y t_y \quad 2\pi k_z = \gamma G_z t_z \tag{2}$$

where G_x and G_y are the phases encoding and G_z the read-out, t(x, y, z) is the duration of the gradients, and γ is the gyromagnetic ratio. Assuming a linear phase evolution as a function of time, the spatial phase shift $\Delta\phi_n(\vec{r}, TE_N)$ can be described by a λth order function across an image voxel as follows:

$$\Delta\phi_n(\vec{r}, TE_N) = i\gamma\Delta TE_N \sum_{K=0}^{\lambda} a_{\lambda-K} r^{\lambda-K} \tag{3}$$

where a is the field map fit coefficients, λ is the fit order, and r is the 3D spatial resolution. ΔTE_N is the echo time difference between the Nth echo and the first echo. In a case where the echo time spacing is fixed, we substitute ΔTE_N with $N.\Delta TE$ where ΔTE is the echo time spacing. The MRI signal can then be rewritten as follows:

$$S_n(k; TE_N) = \int_{-\infty}^{+\infty} \rho_n(\vec{r}, TE_N) \cdot \exp\left\{-2i\pi k\vec{r} + i\gamma N\Delta TE \sum_{K=0}^{\lambda} a_{\lambda-K} r^{\lambda-K}\right\} d\vec{r} \tag{4}$$

2.A. Random temporal phase evolution

Macroscopic field inhomogeneities distort the MRI signal in two ways.[27] Firstly, they can introduce errors when

encoding frequency position during the read-out gradient. This artifact is similar to the chemical shift misregistration observed in the presence of ferromagnetic materials in both spin-echo and GRE sequences. We consider this artifact negligible, however, and its correction not essential for our data. Secondly, if GRE sequences are used, spatial variations in magnetic susceptibility may induce intrinsic magnetic field gradients across image voxels. By applying a radio frequency (RF) pulse, sample protons are brought into synchronous precession, referred to as 'in phase state'. After the RF pulse is switched off, the spinning protons subjected to larger gradients lose phase coherence faster than other protons, leading to image distortion near the air-containing nasal cavity and brain edges.[4,27] This artifact is notably severe in the phase-encode direction and may be removed using different techniques.[19] We should keep in mind that the spatial distortion is more often present in EPI sequences than in normal multi-echo GRE sequences. Conversely, fast signal decay across time remains the main characteristic artifact of quantitative GRE images, and it becomes greater with increasing echo delay after the first RF pulse. This can be explained by the fact that the cumulative loss of phase coherence increases continually and linearly. A linear approximation of dephasing is therefore sufficient for correction. Beyond a certain echo time and in regions subject to large susceptibility differences and low SNR, our simulation and *in vivo* results suggest that the linear trend of phase evolution may be lost. This is consistent with the conclusions drawn by Zeng et al.[19] and Yablonskiy et al.[2] On late echoes, sample protons quickly revert to spinning in random orientation, making the phase behavior appear random. This could be explained by the total loss of phase coherence after a certain delay, with resulting signal loss. Once the protons reach this irreversible random phase state, the phase continues to evolve stochastically with large variation in frequency precessions.

As mentioned earlier, a number of techniques have been proposed to overcome these artifacts present in GRE images. Nevertheless, these techniques have indirectly attempted to solve solely image spatial distortion problems by focusing only on the gradient shape across image voxels (linear, quadratic, etc.). Assuming a linear phase evolution regardless of the gradient amplitude allows only for spatial pixel shift correction and leads inevitably to local signal overcorrection. To accurately account for the fast signal decay with time, which is the main artifact, we should use intrinsic spatial gradient information in conjunction with the temporal phase shift trend. One should keep in mind that the phase has been shown to have a quadratic component in vessels with significant flow and voxels containing multiple water compartments.[28,29] Although the concerned phase shift remains negligible and observable at TE > 100 ms,[28] it can be included in our theoretical framework.

To extend the model further, let us consider that the phase evolution can be described as a combination of linear and random components. We therefore introduce a weighted mixed model that takes into account both linear and stochastic phase behaviors as a function of echo time:

$$\phi_n(\vec{r}, TE_N) = \phi_n(\vec{r}, TE_1) + \mu_n^L \Delta\phi_n(\vec{r}, TE_N) + \mu_n^R \varepsilon_n(\vec{r}, TE_N) \tag{5}$$

The linear term $\Delta\phi_n(\vec{r}, TE_N)$ depicts constant and linear cumulative loss in phase coherence resulting in small signal loss. In contrast, the random term $\varepsilon_n(\vec{r}, TE_N)$ characterizes a stochastic and faster dephasing, which results in overall signal loss. μ_n^L and μ_n^R denote the linear and random coefficients, respectively. Similar to the homogeneity factor, which characterizes the exponential x-ray beam decay, we define the factor 'H' as follows:

$$H = \frac{S(TE_{\frac{3}{4}N})}{S(TE_1)} \tag{6}$$

where $TE_{\frac{3}{4}N}$ represents the echo times taken by the magnitude signal to decay by three-quarters. They can be calculated using the following formula:

$$TE_{\frac{3}{4}N} = -\frac{\ln(3/4)}{R_2^*} \tag{7}$$

This parameter enables us to assess signal decay quality as a function of $B0_{macro}$ inhomogeneities. Based on gray matter R_2^* values reported in the literature,[4,30] $TE_{\frac{3}{4}N}$ was found to be approximately equal to 16 ms. The linear and random factors are therefore defined for a given voxel as:

$$\begin{cases} \mu_n^L = 1 \\ \mu_n^R = 0 \end{cases} \text{if } H > \frac{1}{2} \quad \text{else} \quad \begin{cases} \mu_n^L = 0 \\ \mu_n^R = 1 \end{cases} \tag{8}$$

when $H \leq 0.5$, the signal loses its natural exponential decay and decays much faster than usual, suggesting the presence of large susceptibility differences. When the field gradient inhomogeneities are small ($\mu_n^L = 1$ & $\mu_n^R = 0$), the linear term $\Delta\phi_n(\vec{r}, TE_N) \gg \varepsilon_n(\vec{r}, TE_N)$ dominates the phase evolution and $F_n(\vec{r}, TE_N)$ is well approximated using a linear relationship.[2,17] As the field gradient inhomogeneities become larger ($\mu_n^L = 0$ and $\mu_R = 1$), however, the linear term no longer dominates the phase evolution. The linear relationship no longer holds[19] and the phase jump appears stochastic, until eventually the random component dominates $\Delta\phi_n(\vec{r}, TE_N) \ll \varepsilon_n(\vec{r}, TE_N)$ and the phase behavior appears random. The μ_n^L and μ_n^R coefficients act like a binary mask that splits the brain into two regions, allowing an appropriate phase modeling, and consequently, an adequate correction. Instead of the conventional assumption of linear phase evolution with time regardless of field gradient severity, we use the principles of random walk theory to devise a model describing the phase shift based on the expected temporal variance of the phase dispersion $\sigma_n(\vec{r}, TE_N)$, which can be described as:

$$\sigma_n(\vec{r}, TE_N)^2 = [\langle \phi_n(\vec{r}, TE_N)^2 \rangle - \langle \phi_n(\vec{r}, TE_N) \rangle^2] \tag{9}$$

where $\langle \phi_n(\vec{r}, TE_N) \rangle$ denotes the mean value of the phase signal in time, which tends to the mean value of the phase over echo time $\overline{\phi_n}(\vec{r}, TE_N)$. Analogous to random walk, the mean value $\overline{\phi_n}(\vec{r}, TE_N)$ may be equal to the initial phase value (acquired at N = 1), which means that the probability of finding a voxel phase with a certain value after N echoes is centered

at $\phi_n(\vec{r}, TE_1)$. Naturally, however, the probability distribution widens with increasing numbers of echoes. Because $\overline{\phi_n}(\vec{r}, TE_N)$ is a constant value for each voxel, removing it from the final analytical solution may introduce a constant signal shift over echo times; however, this shift does not affect the signal decay parameters (R_2^*). As such, the expected phase variance can be rewritten as:

$$\sigma_n(\vec{r}, TE_N)^2 = \langle \phi_n(\vec{r}, TE_N)^2 \rangle$$
$$= \sum_{i=0}^{N} \sum_{j=0}^{N} (\langle \omega_{i,n}\omega_{j,n} \rangle \cdot \delta\phi_n(\vec{r}, \Delta TE)^2) \quad (10)$$

where $\omega_{i,j}$ determines the phase variations in time relative to the mean phase value $\langle \phi_n(\vec{r}, TE_N) \rangle$, $\delta\phi_n(\vec{r}, \Delta TE)$ is the mean phase step over time, which can be calculated using Eq. (3), and $(i, j) = 0, 1, 2, 3\ldots N$. To simplify the theory further, the coefficients $\omega_{i,j}$ are defined as:

$$\langle \omega_{i,n}\omega_{j,n} \rangle = \begin{cases} 0, & i \neq j \\ \beta_n, & i = j \end{cases} \quad (11)$$

Thus,

$$\sum_{i=0}^{N} \sum_{j=0}^{N} (\langle \omega_{i,n}\omega_{j,n} \rangle) = N \cdot \beta_n \quad (12)$$

The coefficient β_n can be described using different approaches. In 1D random walk theory, β_n calculation is based on the values that $\omega_{i,j}$ can take. Conventionally $\omega_{i,j} \in [-1,1]$, and consequently β_n will tend to be 1. Based on our simulation, experimental phantom, and *in vivo* studies, however, the phase variations over echo time are larger and consequently, the $\omega_{i,j}$ interval becomes wider. The $\omega_{i,j}$ coefficients are therefore defined as:

$$\begin{cases} \omega_{i,n} = [-\alpha_n, \alpha_n] \\ \omega_{i,n} = \omega_{j,n} \end{cases} \text{ and}$$
$$\alpha_n = abs \left[\frac{Max(\phi_n(\vec{r}, TE_{2 \to N}))}{\phi_n(\vec{r}, TE_1)} \right] \quad (13)$$

Thus,

$$\beta_n = \langle [1, 2, \ldots |\alpha_n|] \rangle \quad (14)$$

where $Max(\phi_n(\vec{r}, TE_N))$ denotes the maximum value of the phase signal over echo time. As highlighted earlier, β_n can be calculated using other methods. In the algebra of random variables,[26] for steps distributed according to any distribution with zero mean and a finite variance (not necessarily a normal distribution), the coefficients β_n can be approximated by the standard deviation of the temporal phase distribution. Nevertheless, introducing additional complex statistical calculations can be computationally intensive for a small benefit. In statistical physics,[24,31] β_n can be approximated by the temporal mean of phase jump, which provides a slightly lower value but remains a simple alternative.

Finally, we can describe the phase shift over the echo time in the presence of small and large $\Delta B_n(\vec{r})$ inhomogeneities as a function of the echo number and β_n, as follows:

$$\phi_n(\vec{r}, TE_N) - \phi_n(\vec{r}, TE_1) = \mu_n^L \Delta\phi_n(\vec{r}, TE_N)$$
$$+ \mu_n^R \varepsilon_n(\vec{r}, TE_N)$$
$$= (\mu_n^L N + \mu_n^R (N\beta_n)^{1/2})$$
$$\cdot \delta\phi_n(\vec{r}, \Delta TE) \quad (15)$$

2.B. Signal correction

The MRI signal can be computed as the inverse Fourier transform (IFT) of the signal $S_n(k; TE_N)$:

$$S_n(\vec{r}, TE_N) = \frac{1}{V_n} \int_k S_n(k, TE_N) \cdot exp\{2i\pi k\vec{r}\}dk \quad (16)$$

where $k_{x,y,z} = 2\pi/\gamma G_{x,y,z}$, $V_n = L_x L_y L_z$ is the voxel volume, and L is the voxel dimension. In order to obtain the analytical IFT expression of the k-space signal, we use some approximations that are valid in high-resolution MRI.[2,32–34] The first approximation assumes that the signal magnitude varies slightly across the voxels. We substitute it with the averaged values across a given voxel:

$$\rho_n(\vec{r}, TE_N) \to \langle \rho(\vec{r}, TE_N) \rangle_n \to \rho_n(TE_N) \quad (17)$$

The second approximation considers that the signal is described by a rectangular function across the voxel dimensions, which reduces the integral in Eq. (1). The IFT of the signal $S_n(k; TE_N)$ after applying the mentioned approximation can be written as:

$$S_n(TE_N) = \frac{1}{V_n} \rho_n(TE_N) \int_{-Lr/2}^{+Lr/2} exp\{-i\gamma(\mu_n^L N + \mu_n^R (N\beta_n)^{1/2})\delta\phi_n(\vec{r}, \Delta TE)\}d\vec{r} \quad (18)$$

Therefore,

$$S_n(TE_N) = \frac{1}{V_n} \rho_n(TE_N) \int_{-Lr/2}^{+Lr/2}$$
$$exp\left\{-i\gamma\Delta TE \sum_{K=0}^{\lambda} a_{\lambda-K} r^{\lambda-K}(\mu_n^L N + \mu_n^R (N\beta_n)^{1/2})\right\}d\vec{r} \quad (19)$$

The third approximation considers that the distribution of the field inhomogeneities evolves slowly through the image voxel. The field gradient, coefficient $a_{\lambda-K}$ in Eq. (3) in our approach, can therefore be computed from the field map by setting $\lambda = 1$ (first-order fit). Thus, when relying on the central difference approximation for field gradient estimates from the in-plane gradients, the remaining artifacts are observed after correction.[2,32,33] Existing solutions based on field map extrapolation beyond air/tissue interfaces[19] or including the through-plane gradients have been demonstrated to improve the field characterization, but these may still lead to inaccurate field estimates and are computationally expensive. We previously introduced a new method to compute the intravoxel gradient as a combination of in-plane and through-plane gradients based on a through-plane projection into the in-plane direction, which

provides a more accurate gradient approximation with greater robustness to edge artifacts.[33] The MRI signal with a linear approximation of the field gradient across the voxel can therefore be described as:

$$S_n(TE_N) = \frac{1}{V_n} \rho_n(TE_N)$$
$$\prod_r L_r \text{sinc}\left(\frac{\gamma}{2}\Delta TE(\mu_n^L N + \mu_n^R (N\beta_n)^{1/2}) \cdot a_{1,n,r} L_r\right)$$

(20)

An additional complication arises because the macroscopic field gradient $a_{\lambda-K}$ can cause voxel dimension distortion (unless the imaging gradient $G_{x,y,z}$ is much stronger).[9,10] In this case, the voxel dimensions must be modified as the true voxel dimensions are no longer L_r, but $\psi_n L_r$,[7,15] where:

$$\psi_n = \frac{G_{x,y,z}}{G_{x,y,z} + a_{\lambda-K}}$$

(21)

Finally, we can describe the MRI signal decay modulated with the 3D Sinc function using both linear approximation and random walk theory to calculate the analytical phase dispersions over echo time as:

$$S_n(TE_N) = \frac{1}{V_n} \rho_n(TE_N)$$
$$\prod_r L_r \text{sinc}\left(\frac{\gamma}{2}\Delta TE(\mu_n^L N + \mu_n^R (N\beta_n)^{1/2}) \cdot a_{1,n,r} \psi_n L_r\right)$$

(22)

To solve this equation and correct for the signal decay caused by the 3D Sinc function modulation, as well as both linear and stochastic phase evolution as a function of echo time, we determine the Sinc function parameters and we divide the image signal by the proposed analytical modulation. We should keep in mind that this approach does not take into consideration the signal phase shift at TE = 0 that results from the RF field inhomogeneities, which is negligible and not essential to correction.

2.C. Weighted field map computation

Conventionally, the phase data are fitted linearly and the field map is calculated by the slope of the fit.[18] Herein, we propose a new approach to compute the field map. The field map is computed as the temporal mean of the unwrapped phase signal tangents as functions of echo times, and weighted by the signal intensity ratio. Similar to the first approximation in Eq. (17), we assume that the phase signal also varies slightly across the voxels. We substitute it with the averaged values across a given voxel:

$$\phi_n(\vec{r}, TE) \rightarrow \langle \phi(\vec{r}, TE) \rangle_n \rightarrow \phi_n(TE)$$

(23)

The field map can be calculated as follows:

$$\Delta B_n = \frac{\Delta \phi_n(\Delta TE)}{N \cdot TE} = \sum_{i=1}^{N} \frac{(\phi_{n,TE1} - \phi_{n,TEi})}{2\pi i \Delta TE} \cdot W_{i.n}$$

(24)

and

$$W_{i.n} = \frac{S_n(TE_i)}{\sum_N S_n(TE_N)}$$

(25)

where n is the voxel coordinates, N is the echo number, and $S_n(TE_N)$ is the signal intensity of the magnitude data in the image domain. Median and Gaussian filters were applied to the weighted field map to reduce the noise in regions with low SNR and remove some phase coil combination artifacts.[13] As the field map values are weighted by the signal intensity ratio $W_{i.n}$, the field estimation is more dependent on the early echoes, which have a better SNR.[35]

3. MATERIALS AND METHODS

3.A. Numerical phantom study

To test our hypothesis and proposed algorithm, we developed a numerical phantom, using customized Matlab scripts (Math Works Inc., Natick, MA), to simulate the effect of $B0_{macro}$. The dataset used in the simulation was generated using the digital brain MRI simulator[36] developed at the Montreal Neurological Institute (Quebec, Canada). It consists of anatomical images segmented into disjoint special masks or templates (one per tissue type). The MR brain properties T_1, T_2^* and PD (gray matter, white matter, and CSF) were set to mimic our real brain data and used to simulate the magnitude signal of a multigradient echo sequence using an analytical solution to the Bloch equation:

$$S_n(TE_N) = \frac{M_{n,0}\exp\left(\frac{-TE_N}{T_2^*}\right)\sin(\alpha)\left(1 - \exp\left(\frac{-TR}{T_1}\right)\right)}{1 - \cos(\alpha)\exp\left(\frac{-TR}{T_1}\right)}$$

(26)

where $M_{n,0}$ is the ideal signal free from the field gradient inhomogeneities and is the flip angle. To evaluate the $B0_{macro}$ effects in more detail and over a wider range than under the experimental conditions, a total of 40 echoes were simulated using the following sequence parameters: $TR/TE_1/\Delta TE = 47/1.23/1.23$ ms, flip angle 10°, and 1 mm² in-plane resolution to limit the field variation across the pixel to a linear behavior. Different degrees of field gradients were introduced by taking a typical field map from an *in vivo* experiment on a 3T scanner. Corrupted magnitude data were subsequently calculated using Eq. (26) multiplied by the function $F_n(\vec{r}, TE_N)$, which describes the signal loss due to $B0_{macro}$. The phase images were then simulated according to Eq. (5), using the first phase image of the *in vivo* field map and modeling the phase noise that depends on the simulated image magnitude as follows:

$$\chi_{phase} = \frac{1}{SNR_{Magnitude}}$$

(27)

where χ_{phase} denotes the introduced phase noise. Equation (27) indicates that voxels with high SNR produce low errors in phase measurement, whereas error in the phase

measurement is large for voxels with low SNR. Errors in the phase maps translate directly to signal loss within voxels.[19] The weighted field map was computed from the simulated phase images according to Eq. (24), and the 3D LS and 3D MMS corrections were performed on the corrupted magnitude images. The computed R_2^* maps were then compared to the true R_2^* values known beforehand. In order to evaluate the qualitative aspect, the Structural SIMilarity (SSIM) is evaluated. The SSIM index can be viewed as a visual quality measure of the simulated images compared to the reference one.[37]

3.B. Experimental phantom and *in vivo* studies

All phantom and *in vivo* scans were performed on a 3T Magnetom Trio (Siemens Healthcare, Erlangen, Germany) using a 32-channel phased array coil. Phantom and *in vivo* images were acquired with a 3D bipolar multigradient echo sequence. Thirty-two echoes were acquired with $TR/TE_1/ \Delta TE = 47/1.23/1.23$ ms, flip angle = 8°, 1.6 mm³ isotropic resolution, a matrix size of $136 \times 136 \times 112$, Grappa parallel imaging with acceleration factor of two, and phase partial Fourier sampling factor of 6/8. The weighted field map was computed from the phase and used as input into the 3D LS and 3D MMS corrections. The performance of the correction algorithms was evaluated using a cylindrical phantom containing five spheres filled with water doped with $MnCl_2$–$4H_2O$ in concentrations of 10, 20, 40, 70, or 120 mg per 1 L of distilled water, in order to examine the linearity of the R_2^* value as a function of manganese concentration.[38] To assess the accuracy of our method, the GRE images from simulation, phantom, and *in vivo* experiments were corrected using our algorithm, which includes random walk theory to describe random phase evolution as a function of echo time and the noniterative version of a postprocessing technique based only on linear phase evolution assumption, described previously.[17,18] In order to compute the R_2^* maps, we extended the numerical trapezoidal integration described previously[39] to utilize Simpson's rule.[40] Thus, the R_2^* maps were computed from both corrected and noncorrected magnitude data, as follows:

$$R_2^* = \frac{S_n(TE_1) - S_n(TE_N)}{\frac{1}{6}(TE_N - TE_1)\left[S_n(TE_1) + S_n(TE_N) + 4S_n\left(\frac{TE_1 + TE_N}{2}\right)\right]}$$
(28)

To further evaluate our approach to correcting field inhomogeneities on real human subjects, we chose 14 samples from scanned *in vivo* data suffering from big signal loss in the paranasal sinuses region and especially in gray matter/air interfaces, and then we corrected the data using both LSC and MMSC. Regions of interest (ROIs) drawn from the selected 14 *in vivo* images near the paranasal sinuses region where the field gradient is large (≥ 50 Hz/cm) after correction with LSC and MMSC were compared with the R_2^* values of ROIs drawn from the center of the brain, where the field inhomogeneities are small (artifact-free or ideal R_2^*).

4. RESULTS

Equation (22) provides an extended theoretical model to account for phase behaviors as a function of echo times, regardless of gradient amplitude. The proposed approach cancels the effects of macroscopic field inhomogeneities through a mixed model combination of the spatial linear intravoxel gradient and its evolution as a function of time.

Figure 1 represents an example of data obtained from a human subject. Figures 1(a) and 1(c) show magnitude images acquired at short (TE = 1.23 ms) and long (TE = 30 ms) echo times, respectively. A ROI is drawn in the presence of low (ROI1: center of the brain) and high (ROI2: paranasal sinuses region) field inhomogeneities. Figure 1(c) illustrates the corresponding field map in Hertz, computed using Eq. (24). Figure 1(d) shows a linear (μ_n^L) and random (μ_n^R) coefficient distribution map, which indicates brain regions corrected either with linear [Eq. (3)] or random approximations [Eq. (11)]. Figure 2 plots an example of unwrapped temporal phase signal histograms from *in vivo* data and simulation (100 samples). Figures 2(a) and 2(b) show results in the region with small (ROI1) and high (ROI2) field inhomogeneity, respectively. Figure 2(c) illustrates how the phase behaves as a function of echo times for one voxel at the very edge of the brain (ROI2). The phase evolution was classified into two time-dependent regimes, linear for TE < 15 ms and random beyond.

In Fig. 3, we present results of a simulation study obtained using a numerical brain phantom. In order to assess the performance of algorithms over a wider range than that available under experimental conditions, the data were corrupted by introducing a severe field gradient across image voxels (> 100 Hz/cm).

Figure 4 shows the resulting R_2^* maps obtained in the phantom study without correction and after correction using LSC or MMSC, respectively. The arrows indicate regions suffering from high macroscopic field inhomogeneities around spherical air bubbles and near phantom edges.

In Fig. 5, R_2^* values in Hertz are plotted as a function of M_nCl_2 concentrations in mg/L within the phantom spheres, before and after correction using both LSC and MMSC, respectively. Figure 6 presents boxplots of R_2^* values from 14 human subjects. A ROI drawn in the paranasal sinuses (gray and white matter) region shows a large field gradient (≥ 50 Hz/cm) after correction using LSC and MMSC, whereas the R_2^* values of a ROI drawn in the center of the brain show small field inhomogeneities (artifact-free or ideal R_2^*). To locally evaluate the LSC and MMSC techniques, different brain volumes were derived from the MPRAGE image using in-house software based on variational expectation-maximization tissue classification.[41] The following regions were automatically segmented: whole-brain white matter (WM), cortical gray matter (GM), thalamus, basal ganglia (caudate, putamen, and globus pallidus), and cerebellar WM and GM. Figure 7 shows the distribution of T_2^* ($1/R_2^*$) histograms in the above-mentioned segmented brain regions. Figure 8(a) presents a R_2^* map without any corrections for the
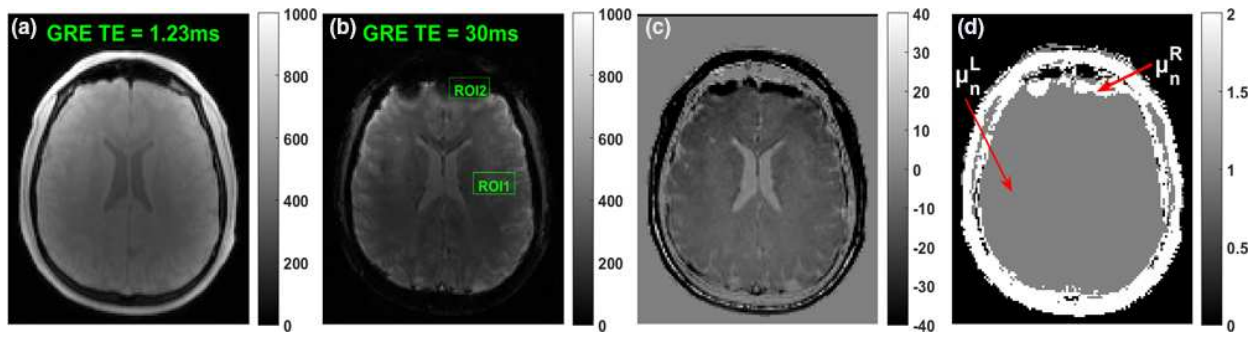
FIG. 1. Example of data obtained from a single human subject. GRE magnitude images are acquired at short (a) and long (b) echo times to highlight the susceptibility-induced macroscopic field inhomogeneities. (c) The corresponding field map (Hz), where strong field gradients are visually observed at air/tissue interfaces (paranasal sinuses region) and near edges. (d) A linear (μ_n^L) and random (μ_n^R) distribution map, which splits brain into two regions and applies the corresponding correction. [Color figure can be viewed at wileyonlinelibrary.com]
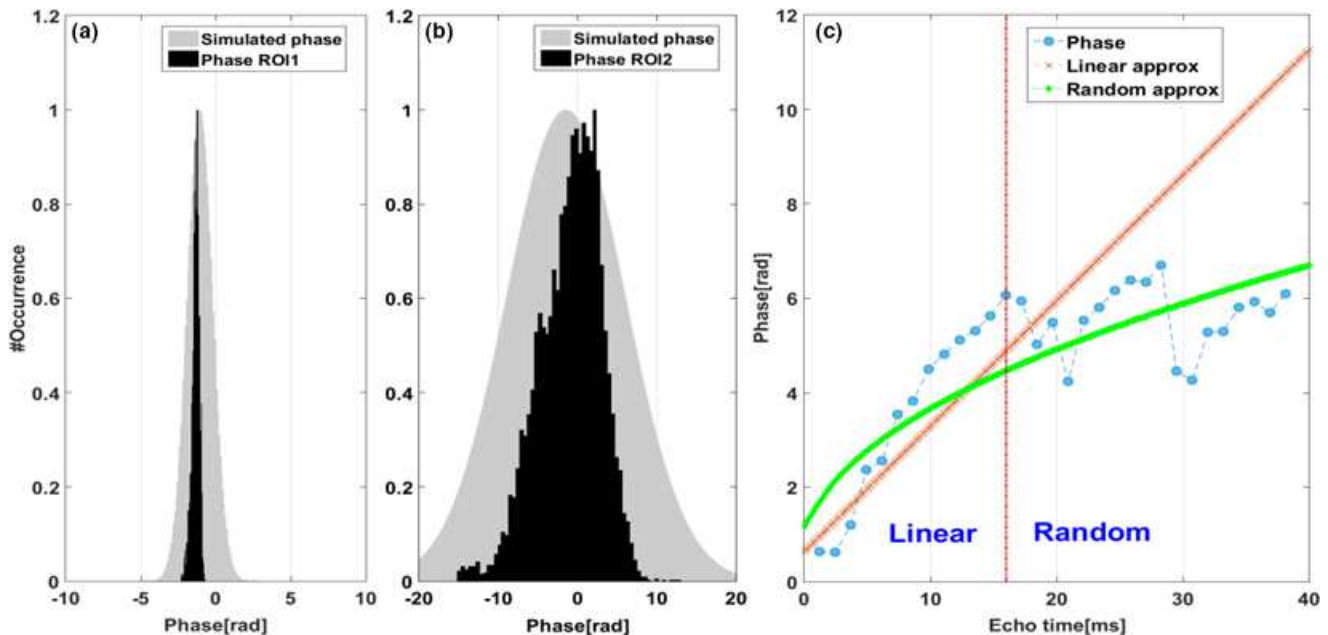

FIG. 2. Example of unwrapped temporal phase data obtained from a single human subject. Simulated and measured phase distribution histograms are shown in the presence of low (a) and high (b) macroscopic field gradient. (c) An example of voxel phase behavior as a function of time in the presence of high field inhomogeneities (voxel within ROI2). It is clear that phase loses linearity after a certain time and behaves stochastically. The phase after N echoes is approximated using both linear (dashed with cross markers red line) and random (solid green line) approaches. [Color figure can be viewed at wileyonlinelibrary.com]

macroscopic field inhomogeneity. One can clearly observe the R_2^* overestimation in the paranasal sinuses region, where the field gradient is high, as well as near the brain edges. Figures 8(b) and 8(c) show R_2^* maps corrected using LSC and MMSC, respectively.

5. DISCUSSION

The simulation and *in vivo* studies presented in this work demonstrate the main features of the proposed method. Susceptibility-induced macroscopic field inhomogeneity artifacts increase with increasing echo time (Fig. 1). The presence of air, which has a low susceptibility due to its low density,[27] produces a large susceptibility difference at the tissue interfaces. An additional significant

susceptibility difference may be created between the gray matter and skull. Areas subjected to severe field gradients suffer from image distortion and faster signal loss with echo time. In Fig. 1(c), one can clearly observe that large frequency shifts ($|\Delta B| > 40$ Hz) are highly present in regions near the paranasal sinuses and at the very edge of the brain. Nevertheless, far from these regions, field inhomogeneities are negligible (e.g., center of the brain). Based on this information, in conjunction with signal quality decay as a function of time, the proposed algorithm splits the brain into two different regions depending on the correction to be applied. MMSC applies a random phase approximation to regions near the paranasal sinus cavity and the brain extremities, which is in good agreement with the field gradient distribution shown in the corresponding
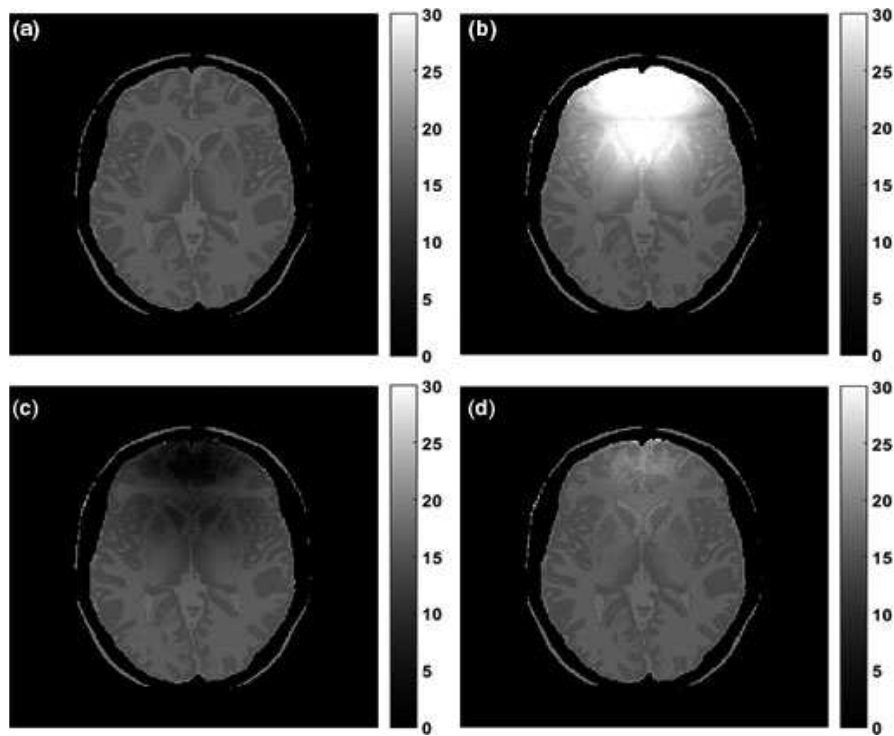
FIG. 3. Simulation results of R_2^* maps corrected with LSC and MMSC. (a) Original R_2^* map (Hz), (b) Corrupted map without correction, (c and d) R_2^* map after application of LSC and MMSC, respectively.
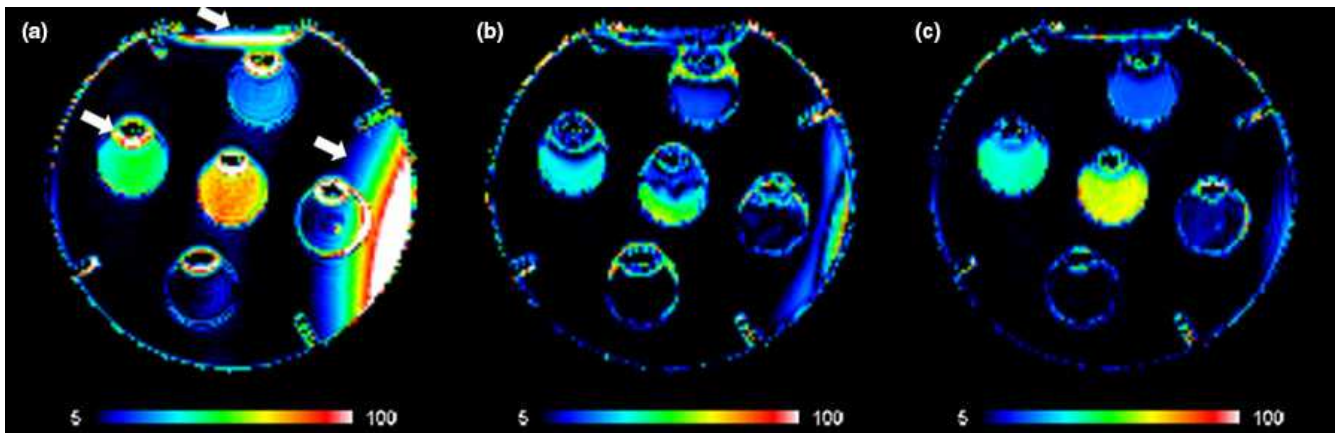

FIG. 4. (a) Phantom R_2^* map (Hz) without correction, (b) and (c) same map with LSC and MMSC correction, respectively. The arrows show regions suffering from high macroscopic field inhomogeneities. [Color figure can be viewed at wileyonlinelibrary.com]

field map [Fig. 1(d)]. Elsewhere, MMSC utilizes a linear approximation and applies the conventional correction.

In Fig. 2, evidence of random phase behavior in the presence of large field gradient inhomogeneities is presented. Figure 2(a) plots the phase distribution histogram for the ROI drawn in the center of the brain. Far from field inhomogeneities, the histogram appears narrow within a tight range, indicating a small and steady temporal phase shift evolution. In Fig. 2(b), the phase histogram appears wider and may be fitted to a normal or a Gaussian distribution. This symmetrical normal distribution about the mean phase typically characterizes a random variable,[25] which in our case represents

the temporal phase behavior. The simulations were in good agreement with experimental measurements in both cases. In the presence of a large macroscopic field gradient, the phase evolves in a linear manner until a certain echo time. Unlike what is conventionally thought, beyond this echo time limit, the linear assumption is broken [Fig. 2(c)]. These results are in agreement with those reported in Ref. [19]. Assuming a simple linear phase evolution with time is no longer valid; therefore, using a linear model to describe the phase behavior (dashed with cross markers red line fit) overestimates the real value of the temporal phase shift. As explained in the *Theory* section above, to achieve an ideal correction, one should
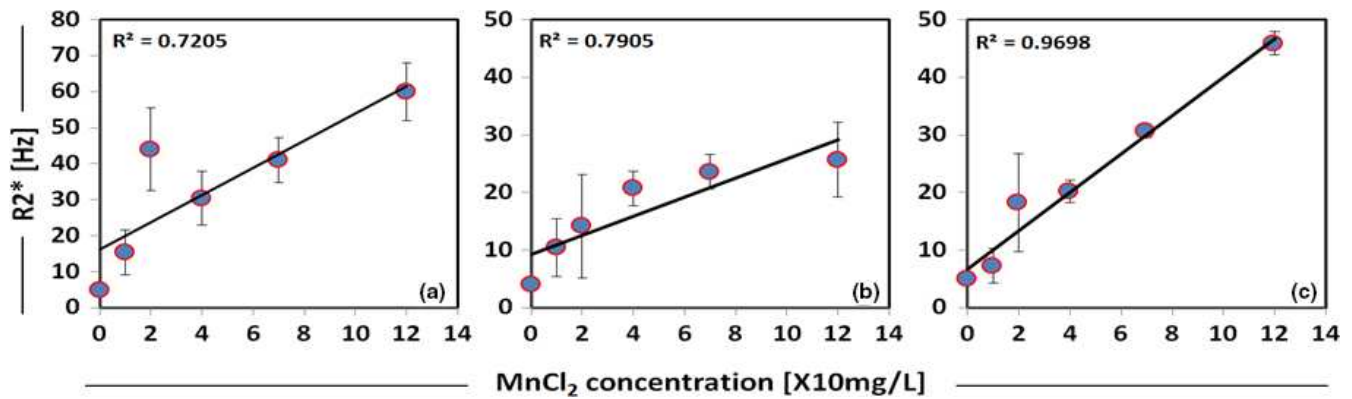
FIG. 5. R_2^* value (Hz) as a function of M_nCl_2 concentrations (mg/L) within the phantom spheres, before (a) and after correction with both LSC (b) and MMSC (c). [Color figure can be viewed at wileyonlinelibrary.com]
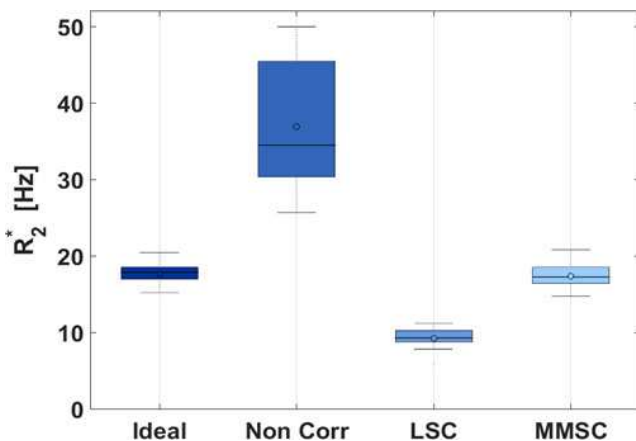

FIG. 6. Boxplot of R_2^* values for 14 *in vivo* studies. ROI drawn in the paranasal sinuses region where the field gradient is large (≥ 50 Hz/cm) after correction with LSC and MMSC, compared with the R_2^* values of ROI drawn in the center of the brain where the field inhomogeneities are small (artifact-free or ideal R_2^*). Lower and upper boundary lines are at the 25%/75% quantile, and the central line and circle indicate the data median and mean values, respectively. MMSC recovers the R_2^* values with high accuracy and less noise compared to LSC method, which tends to underestimate the R_2^*. [Color figure can be viewed at wileyonlinelibrary.com]

correctly combine the spatial phase shift across a voxel, which provides information about the spatial intensity distortion, with the temporal phase shift, which characterizes gradient severity across time. Hence, MMSC partially based on the random walk theory remains by far the best method, as it describes precisely the temporal phase evolution (solid green line fit) and provides an analytical solution for artifact correction.

Figure 3 shows the simulated corrupted R_2^* map with a severe gradient field before and after correction using the previously mentioned methods. By using a digital brain phantom with reasonable quantitative values, our objective was to generate a sensible simulation study producing realistic artifacts. Large gradient inhomogeneities were introduced in the frontal sinus, superior frontal gyrus, and cingulate region. Despite the lack of realism regarding the spatial field distribution, the simulated artifact was identical to the real one. Without

correction, R_2^* is overestimated by more than 100%, and the biological information and brain structures are lost. In the center of the brain, where the field gradient is less than 2 Hz/cm, both LSC and MMSC provide approximately the same correction. In the presence of large field inhomogeneities, however, LSC overestimates the correction and thus underestimates R_2^* values, whereas MMSC appears more robust and provides a more accurate correction. The R_2^* map is corrected with an accuracy of 4 Hz and the brain structures are well recovered.

It is important to point out that in regions with high SNR and in the absence of ferromagnetic metallic objects, quantitative R_2^* correction remains small and can be achieved by either method. Potentially, there is no benefit for correcting such regions and any applied correction may introduce additional errors rather than improving the estimates. Conversely, when the field gradient is large, the simulations showed that the free induction decay signal (FID) drops abruptly with large Sinc modulation when using the LSC model, which in reality does not appear on magnitude data. Consequently, the signal correction is overestimated and the R_2^* values are underestimated. MMSC showed a moderated and uniform FID exponential decay, which better reflects the susceptibility-induced signal drop seen in GRE images. In regions with a large field gradient, the computed Structural SIMilarity index (SSIM)[37] remains under 0.7 when correcting data with LSC; however, the index increases and becomes high (0.95–1) when MMSC is applied. This enables us to conclude that, in addition to the quantitative R_2^* parameter recovery, MMSC also recovers the visual quality of the image structure, with noise reduction affecting the qualitative aspects.

The presence of M_nCl_2 causes the signal to decay quickly and the presence of air bubbles creates strong magnetic field inhomogeneities, which leads to a substantial increase of R_2^* (Fig. 4). One can observe that R_2^* values are overestimated near the phantom edges and around the air bubbles. A large gradient artifact is observed on the right side of the phantom. The LSC technique reduces field inhomogeneity artifacts in regions with high SNR (SNR ≥ 10), but the correction leads to R_2^* underestimation around the air bubbles. Phantom side artifacts and near edge R_2^* overestimation are only partially
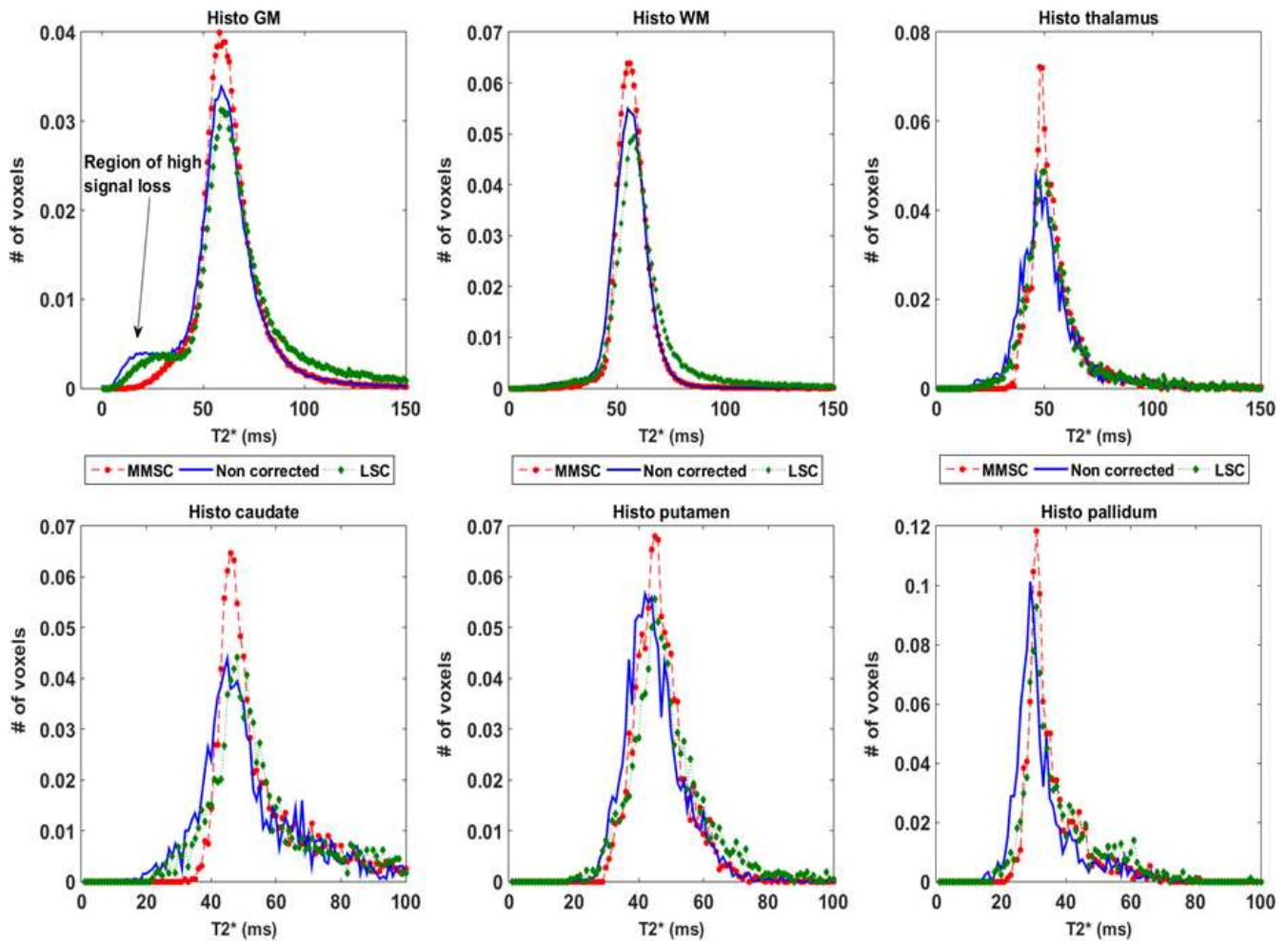
FIG. 7. R_2^* histograms of segmented brain regions of the *in vivo* data of a single human subject, including the gray matter (GM), normal-appearing white matter (NAWM), thalamus, caudate, putamen, and pallidum. MMSC removes the artifactual regions from all brain segments, particularly from the GM where air/tissue interfaces are larger near the paranasal sinuses and frontal lobe (arrow). [Color figure can be viewed at wileyonlinelibrary.com]

removed. MMSC provides a similar correction in regions with high SNR and also provides a realistic correction in regions with low SNR (SNR ≤ 4). Accounting for both intra-voxel dephasing and temporal phase shift using our method enables R_2^* overestimation to be substantially reduced within the spheres and near the phantom edges, as well as reducing the artifact visible on the left side of the phantom.

It is well known that R_2^* values increase linearly with increasing M_nCl_2 concentration.[38] We plot the mean R_2^* values against M_nCl_2 concentrations (Fig. 5). Without correction, poor linearity ($R^2 = 0.72$) is observed between the R_2^* estimates and M_nCl_2 concentration, especially for a concentration of 20 mg/L, which is a clear artifact. At low concentrations, both corrections are similar and appear to remove the R_2^* overestimation for the sphere containing 20 mg/L of M_nCl_2. With increasing M_nCl_2 concentrations (≥ 40 mg/L), however, the LSC method results in larger correction of the R_2^* estimate, which then loses the linear relationship with M_nCl_2 concentration. Overall, this over-correction does not enhance R_2^* linearity ($R^2 = 0.79$), even if a good correction is performed for small M_nCl_2

concentrations. In comparison with the MMSC method, the proposed approach provides an optimal R_2^* correction and maintains linearity at high M_nCl_2 concentrations, considerably improving it ($R^2 = 0.97$).

Similar to the phantom study, the presence of large macroscopic field gradient inhomogeneities in specific regions, such as the paranasal sinuses, around the cingulate, and near the brain edges (SNR ≤ 4), leads to image distortion and temporal signal loss, which results in an overestimation of R_2^* values (Fig. 8). In the center of the brain (SNR ≥ 10), field inhomogeneities are less significant and both LSC and MMSC provide the same correction.

In Fig. 6, one can observe that without correction, the quantitative R_2^* parameters are overestimated. In our *in vivo* studies, the ideal R_2^* mean value was equal to 17.6 Hz, which is not far from the values previously reported in the literature.[4,30] These quantitative values increase by 100% in the presence of severe susceptibility artifacts. MMSC performs very well, yielding a mean R_2^* of 17.3 Hz, which is consistent with values computed in homogeneous areas with an error of less than 1%. As expected, LSC overcorrects the data and
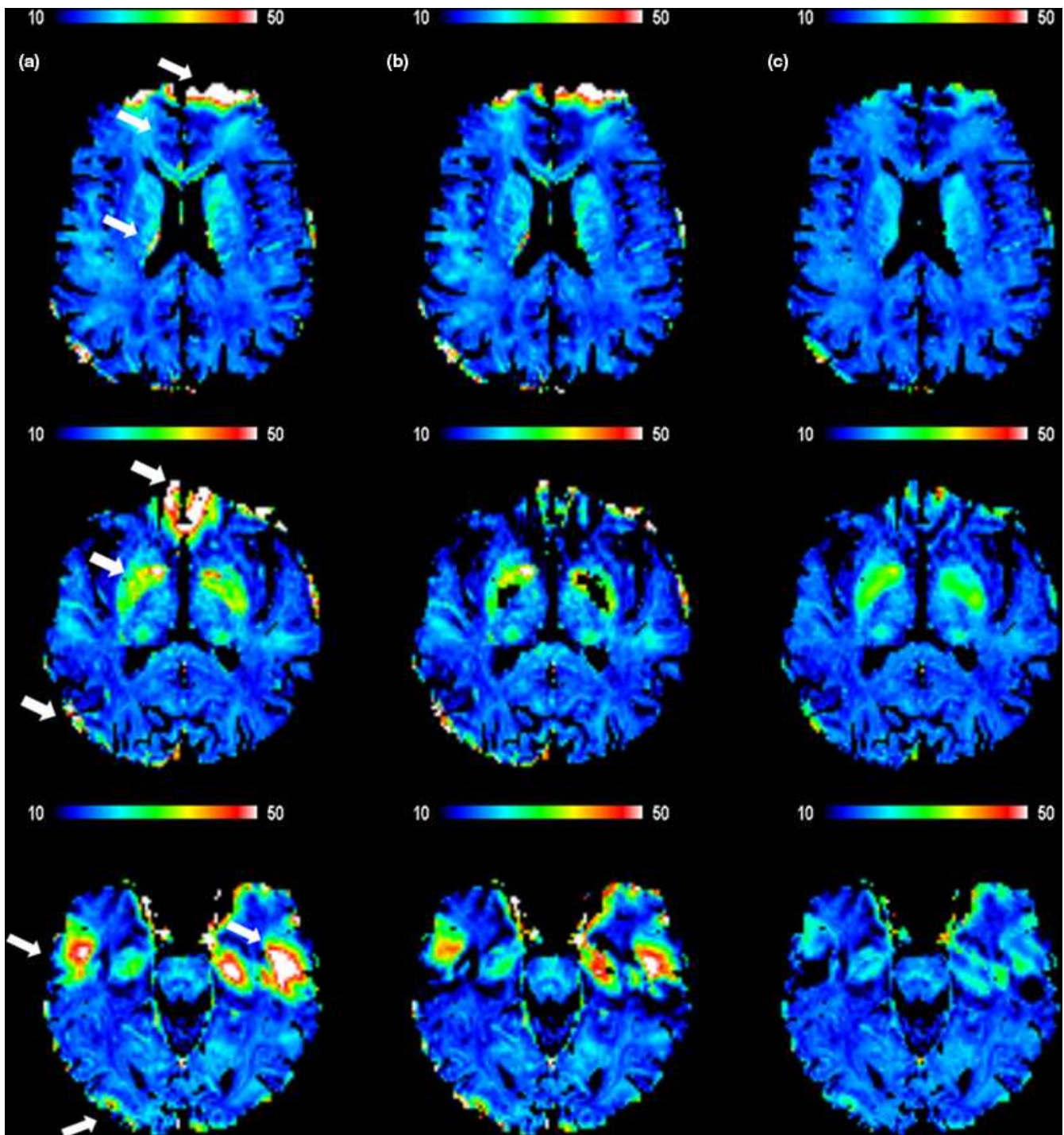
FIG. 8. Example of *in vivo* data obtained from a single human subject. (a) Three representative slices of R_2^* map (Hz) without correction. (b) and (c) R_2^* maps corrected using LSC and MMSC, respectively. The arrows show regions suffering from high macroscopic field inhomogeneities. [Color figure can be viewed at wileyonlinelibrary.com]

achieves a mean R_2^* of 9 Hz, thus underestimating the signal by approximately 40%.

MMSC removes the artifactual regions from all segmented brain parts, particularly the normal-appearing white matter (NAWM) and GM histograms (Figs. 7 and 8, indicated by arrows). LSC fails in this respect, however, because of the linear approximation of the phase behavior as a function of time

and the lack of information regarding the field gradient near the brain edges.

The simulation and *in vivo* results showed difficulties in estimating the field map in the presence of large susceptibility artifacts. The phase behaves linearly in the presence of a low field gradient, but as soon as the field gradient increases, the linearity is lost. In Ref. [2], it was suggested that only

short TE can be used for evaluation of the field map. We believe, however, that accounting for echoes at long TEs may add precious information concerning the severity of gradient evolution with time. It is well known that large echo spacing (ΔTE) and long repetition time (TR) may account for undesired phase wraps and image quality degradation (low SNR). In this work, we briefly introduced a weighted field map method that provides accurate field map estimation, even in the presence of low SNR and nonlinear phase behavior. The approach provides a real-time computation regardless of the number of echoes used. A description of the weighted field map method is beyond the scope of this work and will be discussed in future work.

Gradient computation near the brain edges is described as a limitation to R_2^* correction. Existing solutions based on field map extrapolation beyond air/tissue interfaces[11] or computing the gradient for the left-sided neighbor[2] have been demonstrated to improve the field characterization, but may still lead to inaccurate field estimates and are computationally expensive. Introducing this fast through-plane gradient computation method removes the gradient overestimation; however, while correcting the R_2^* maps without a large increase in computation time.

The approximations used to build the algorithm, such as the ideal slice profile and the linear field variation across the image voxel, are valid in isotropic high-resolution imaging. Extra field behavior measurements showed no benefit from increasing polynomial fit order or voxel neighbor size while using high-resolution images. In the case of low-resolution images, the linear intravoxel gradient approximation changes and may be replaced by a quadratic or higher field characterization,[3,20] although the nonlinear phase behavior remains valid and the phase dispersion can be computed using the proposed approach. The combination of MMSC and nonlinear field gradient evolution across the image voxel will be investigated in the future for low-resolution imaging (slice thickness > 3 mm).

In this work, all data were acquired using a bipolar, multi-gradient echo sequence. This technique enables us to easily perceive and characterize pathologies, such as iron overload disorders. At the same time, however, it causes phase errors that may result from eddy currents, as well as gradient delays that can vary for different gradient lobes. If the image voxel contains a mixture of tissues, a phase cancelation effect may occur, disturbing the inter-echo phase consistency and leading to white or black rim appearance in regions near the brain edges. Nonetheless, if the magnitude of signal modulation is known, it can be removed by postprocessing during quantitative R_2^* computation form the corrected magnitude data. We have previously demonstrated that the ringing artifact may be successfully removed from both magnitude and R_2^* images using odd even modulation correction, described in Ref. [40], without any spatial resolution loss, which is the case when spatial smoothing filters are applied (e.g., median or Hanning filters).[2]

The computation of the MMSC in Matlab took less than 2 min on a standard PC, and programming in C/C++ would allow further reduction of computation time. The MMSC postprocessing correction procedure can therefore be implemented to correct macroscopic field distortion in real time.

The correction of macroscopic field inhomogeneities can be used in different applications. As a next step, we will investigate the effect of field inhomogeneities correction on the detection of iron deposits. It is well known that iron deposition (hemosiderin) can lead to field distortion around a lesion (Blooming artifact). Consequently, the bleeding area appears larger.[42] To this end, we aim to compare the size of iron deposit lesions from R_2^* maps with and without the use of LSC and MMSC, to MP2RAGE images, which are less sensitive to the B0$_{macro}$ field.[43]

Another potential application of R_2^* correction would be further investigation of the detection of microbleeds, and validation of the cut-off point assumption to distinguish between macro- and microbleeds in patients with intracerebral hemorrhaging.

The SWI technique, produced by multiplying the R_2^*-weighted gradient echo magnitude and filtered phase images, has enormous potential for assessing brain iron content.[4,6] If extended from a single echo to multiple echoes, both R_2^* and SWI maps may be acquired in a single scan[4]. Unlike iterative algorithms, our approach computes R_2^* parameters after correcting magnitude images. Thus, it can be used to enhance SWI by recovering the signal caused by macroscopic field inhomogeneities near the sinus cavity and at brain edges.

6. CONCLUSION

A large number of studies have focused on solving the problem of R_2^* correction due to macroscopic field inhomogeneities. The complexity of the problem, however, has left an open field requiring further research and development efforts. In this work, we proposed a new approach to correct the quantitative R_2^*, which we consider to be a significant advancement in the field. To date, earlier studies devoted to solving the problem have considered only field gradient shape and strength across voxels as the main phenomena behind signal loss, neglecting the temporal phase shift behavior by assuming a linear temporal phase evolution, regardless of the gradient amplitude. In the presence of large field gradients, however, such as near the edge of the brain, this assumption is no longer valid and the phase evolution appears random. Field gradient inhomogeneities affect images in two distinct ways: spatial pixel intensity shift and fast temporal signal loss. The first artifact is characterized by the strength of the intrinsic gradient across voxels. Hence, temporal signal loss is correlated with temporal phase shift evolution. Only accurate conjunction of the two facts allows a precise correction. We therefore reconsidered the basic theory and developed an analytical mixed model for phase dispersion estimation over echo time, which takes into account both linear and stochastic temporal phase behaviors. The proposed technique shows promise for improving R_2^* measurements regardless of the severity of gradient inhomogeneities. Clinical and research applications require further investigation.

ACKNOWLEDGMENTS

CONFLICT OF INTEREST

The authors declare that they have no conflicts of interest.

[a)]Author to whom correspondence should be addressed. Electronic mails: chems.fatnassi@hirslanden.ch, chemsfatnassi@hotmail.fr; Tel: +41 21 619 68 48.

REFERENCES

1. Yablonskiy DA. Quantitation of intrinsic magnetic susceptibility related effects in a tissue matrix: phantom study. *Magn Reson Med*. 1998;39:417–442.

2. Yablonskiy DA, Alexander L, Luo SJ, Wang X. Voxel spread function method for correction of magnetic field inhomogeneity effects in quantitative gradient echo based MRI. *Magn Reson Med*. 2012;70:1283–1292.

3. Yang X, Sammet S, Schmalbrock P, Knopp M. Post-processing correction for distortions in T2* decay caused by quadratic cross slice B0 inhomogeneity. *Magn Reson Med*. 2010;63:1258–1268.

4. Denk C, Rauscher A. Susceptibility weighted imaging with multiple echoes. *J Magn Reson Imaging*. 2009;31:185–191.

5. Haacke E, Cheng N, House M, et al. Imaging iron stores in the brain using magnetic resonance imaging. *Magn Reson Med*. 2005;23:1–25.

6. Shmueli K, de Zwart JA, van Gelderen P, Li T, Dodd SJ, Duyn JH. Magnetic susceptibility mapping of brain tissue in vivo using MRI phase data. *Magn Reson Med*. 2009;62:1510–1522.

7. Anderson L, Holden S, Davis B, et al. Cardiovascular T2-star T2* magnetic resonance for the early diagnosis of myocardial iron overload. *Eur Heart J*. 2001;22:2171–2179.

8. Wood J, Enriquez C, Ghugre N, et al. MRI R2 and R2* mapping accurately estimates hepatic iron concentration in transfusion-dependent thalassemia and sickle cell disease patients. *Blood*. 2005;106:1460–1465.

9. Gati J, Menon R, Ugurbil K. Experimental determination of the bold field strength dependence in vessels and tissue. *Magn Reson Med*. 1997;38:296–302.

10. Zwaag WV, Francis S, Head K, et al. fMRI at 1.5, 3 and 7 T: characterizing bold signal changes. *NeuroImage*. 2009;47:1425–1434.

11. Grandin C. Assessment of brain perfusion with MRI: methodology and application to acute stroke. *Neuroradiology*. 2003;45:755–766.

12. Wirestam R, Thilmann O, Knutsson L, Burtscher IB, Larsson E, Stahlberg F. Comparison of quantitative dynamic susceptibility contrast MRI perfusion estimates obtained using different contrast agent administration schemes at 3T. *Eur J Radiol*. 2010;75:86–91.

13. An H, Lin W. Impact of intravascular signal on quantitative measures of cerebral oxygen extraction and blood volume under normo and hypercapnic conditions using an asymmetric spin echo approach. *Magn Reson Med*. 2003;50:708–716.

14. Kolliaa K, Maderwalda S, Putzkib N, et al. First clinical study on ultrahigh field MR imaging in patients with multiple sclerosis: comparison of 1.5T and 7T. *AJNR Am J Neuroradiol*. 2009;30:699–702.

15. Frahm J, Merbold K, Hanick W. Direct flash MR imaging of magnetic field inhomogeneities by gradient compensation. *Magn Reson Med*. 1988;6:474–480.

16. Baudrexel S, Volz S, Preibisch C, et al. Rapid single scan T2* mapping using exponential excitation pulses and image based correction for linear background gradient. *Magn Reson Med*. 2009;62:263–268.

17. Seara MF, Wehrli F. Post processing technique to correct for background gradients in image-based R2* measurements. *Magn Reson Med*. 2000;44:358–366.

18. Dahnke H, Schaeffter T. Limits of detection of SPIO at 3.0 T using T2 relaxometry. *Magn Reson Med*. 2000;62:1202–1206.

19. Zeng H, Constable RT. Image distortion correction in EPI: comparison of field mapping with point spread function mapping. *Magn Reson Med*. 2005;48:137–146.

20. Hernando D, Vigen K, Shimakawa A, Reeder S. R2* mapping in the presence of macroscopic B0 field variations. *Magn Reson Med*. 2010;68:830–840.

21. Fatnassi C, Boucenna R, Zaidi H. Unwrapping highly wrapped phase using nonlinear multi-echo phase unwrapping. *IFMBE Proc*. 2015;51:115–118.

22. Kittel C. Solid state physics; 2005.

23. Spitzer F. Principles of random walk; 2001.

24. Kardar M. *Statistical Physics of Particles*. New York: Cambridge University Press; 2007.

25. Casella G, Berger R. *Statistical Inference*, 2nd edn. Pacific Grove, CA: Duxbury Press; 2001.

26. Springer DM. The algebra of random variables; 1979.

27. Czervionke LF, Daniels DL, Wehrli FW, et al. Magnetic susceptibility artifacts in gradient-recalled echo MR imaging. *Am J Neuroradiol*. 1988;9:1149–1155.

28. Robinson S, Schödl H, Trattnig S. A method for unwrapping highly wrapped multi-echo phase images at very high field: UMPIRE. *Magn Reson Med*. 2013;71:80–92.

29. Wharton S, Bowtell R. Fiber orientation-dependent white matter contrast in gradient echo MRI. *Proc Natl Acad Sci USA*. 2012;109:18559–18564.

30. Krüger G, Glover GH. Physiological noise in oxygenation-sensitive magnetic resonance imaging. *Mag Reson Med*. 2001;46:631–637.

31. Kardar M. Statistical physics of fields; 2007.

32. Fatnassi C, Kreuger G, Meuli R, O'Brien K. Nonlinear correction of R2* maps from macroscopic field inhomogeneities. *Proc Eur Soc Magn Reson Med Bio*. 2013;26:234–235.

33. Fatnassi C, Kreuger G, Meuli R, O'Brien K. Nonlinear correction of 3D R2* maps with fast through-plane gradient mapping computation. *Proc Intl Soc Mag Reson Med*. 2014;22:1645.

34. Fatnassi C, Boucenna R, Betz M, Zaidi H. Correction of macroscopic field inhomogeneities in 3D quantitative GRE imaging based on nonlinear phase model and SNR mapping. *Proc Intl Soc Mag Reson Med*. 2015;23:3766.

35. Irarrazabal P, Meyer HC, Nishirnura GD, Macovski A. Inhomogeneity correction using an estimated linear field map. *Magn Reson Med*. 1996;35:278–282.

36. Kwan RKS, Evans AC, Pike GB. MRI simulation-based evaluation of image-processing and classification methods. *IEEE Trans Med Imaging*. 1999;18:1085–1109.

37. Wang Z, Bovik AC, Sheikh HR, Simoncelli EP. Image quality assessment: from error visibility to structural similarity. *IEEE Trans Image Process*. 2004;13:600–612.

38. Timothy G, Pierre S, Clark RP, et al. Noninvasive measurement and imaging of liver iron concentrations using proton magnetic resonance blood. *Magn Reson Med*. 2005;105:855–861.

39. Hagberg G, Indovina I, Sanes J, Posse S. Real-time quantitation of T2* changes using multi echo planar imaging and numerical methods. *Magn Reson Med*. 2002;48:877–882.

40. Fatnassi C, Boucenna R, Zaidi H. Numerical Simpson's rule for real time and accurate T2* maps generation using 3D quantitative GRE. *IFMBE Proc*. 2015;51:107–110.

41. Roche D, Ribes M, Bach Cuadra M, Kruger G. On the convergence of EM-like algorithms for image segmentation using Markov random fields. *Med Image Anal*. 2011;15:830–839.

42. Greenberg SM, Ernooij MW, Cordonnier C, et al. For the microbleed study group. Cerebral microbleeds: a guide to detection and interpretation. *Lancet Neurol*. 2009;8:165–174.

43. Marques PJ, Kober T, Krueger G, Van der Zwaag W, De Moortele PFV, Gruetter R. MP2RAGE, a self-bias-field corrected sequence for improved segmentation and T1 mapping at high field. *NeuroImage*. 2010;49:1271–1281.